

Joint Estimation of Bulk Flow Velocity and Angle Using a Lateral Line Probe

Nataliya Strokina, Joni-Kristian Kämäräinen, Jeffrey A. Tuhtan, Juan F. Fuentes-Pérez, and Maarja Kruusmaa

Abstract—The measurement of complex natural flows, especially those occurring in rivers due to man-made structures is often hampered by the limitations of existing flow measurement methods. Furthermore, there is a growing need for new measurement devices which are capable of measuring the hydrodynamic characteristics of complex natural flows required in environmental studies which often use fish as an indicator of ecological health. In this work, we take the first step towards in-situ natural flow measurements with a new biologically-inspired probe design in conjunction with signal processing methods. The device presented in this work is a dedicated hydrodynamically sensitive sensor array following the fish lateral line sensor modality. Low-level, multi-dimensional sensor signals are transformed to the two key hydrodynamic primitives, bulk flow velocity and bulk flow angle. We show that this can be achieved via a canonical signal transformation and kernel ridge regression, allowing for velocity estimates with less than 10 cm/s error. The approach provides robust velocity estimates not only when the sensor is ideally oriented parallel to the bulk flow, but across the full range of angular deviations up to a completely orthogonal orientation by correcting the pressure field asymmetry for large angular deviations. Furthermore, we show that their joint estimation becomes feasible above a threshold current velocity of 0.45 m/s.

Index Terms—bio-inspired flow sensing, artificial lateral line, flow velocity, flow angle, flow measurements

I. INTRODUCTION

QUANTITATIVE evaluation of complex natural flows, especially in rivers has become an important issue as poorly functioning hydraulic structures can be detrimental for ecosystem development. New measurement devices and data processing workflows are required which are capable of measuring the complex in-situ hydrodynamic conditions in order to catalog natural flow characteristics which can then be used to improve existing structures and optimize current design standards.

In this work, we take the first step toward bio-inspired flow measurement and propose a new probe design and signal processing workflow capable of in-situ measurements of complex hydrodynamic flow patterns. An ideal physical description of a flow pattern would require simultaneous measurement of velocity, vorticity, and pressure at minute spatial and temporal resolutions which is not feasible. Compared to contemporary flow measuring techniques, the lateral line probe introduced in this work is robust enough for field measurements, achieves

high data acquisition rates, and can be used to estimate both current velocity and angle. The lateral line organ – “touch-at-a-distance” – [29] is a unique sensor modality rarely exploited in sensor applications which provides information about the chaotic and complex fluid-body interaction and is used for tasks such as stable locomotion in turbulent environments, economic diving by flow adaptation, and hydrodynamic imaging of flow patterns required for prey and obstacle recognition. The physiological structure and signal responses of the lateral line are actively investigated in biology [7], [27] and several attempts to build an artificial lateral line have been reported [48], [47], [43], [34]. In this work, we propose a lateral line based flow sensing probe which experiences flows analogous to a biological lateral line structure, focusing on signal processing rather than the mechanical response of the biological sensor.

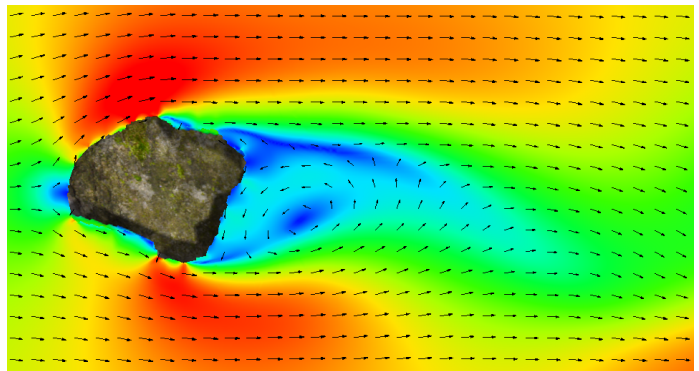


Figure 1: Example “spatial flow map” showing the distribution of flow velocity and flow direction - “local flow patterns”.

By relaxing the constraints imposed on previous works studying the biological and mechanical sensitivity of the lateral line, we are able to leverage the sensor system’s lateral line modality in a much more affordable way, using only commodity hardware parts. Our probe provides a multi-dimensional sensor signal (each dimension corresponds to a single sensor in the array) for which we propose a signal processing workflow for two key flow pattern primitives: i) bulk flow angle and ii) bulk flow velocity. The effectiveness of the lateral line probe to solve these tasks is demonstrated using ridge regression, which takes the raw sensor array signal as input and outputs the flow angle or velocity. The joint detection of both is essential for field measurements and we propose a signal processing pipeline which first estimates the bulk flow angle and then carries out a computational transformation to a “canonical space”. In canonical space, the input signal is invariant to

N. Strokina and J.-K. Kämäräinen are with the Department of Signal Processing, Tampere University of Technology, Finland, e-mail: first-name.lastname@tut.fi.

J. Tuhtan, J.F. Fuentes-Pérez, and M. Kruusmaa are with the Center of Biorobotics, Tallinn University of Technology, Estonia.

J. Tuhtan is also with SJE Ecohydraulic Engineering GmbH

the unknown (but estimated) angle and is used to estimate the bulk velocity. One drawback of this approach is the calibration requirement, which is also discussed and analyzed in detail. Ridge regression provides computationally inexpensive real-time execution and the proposed methods are generic in the sense that they can be applied with different artificial lateral line sensor configurations. We demonstrate the accuracy and robustness of the sensor to angular deviations from the ideal orientation using signal processing pipeline based on data taken from laboratory experiments under fully turbulent flow conditions. The methods are devised for ego-centric measurements in arbitrary pose and are therefore referred to as “local flow sensing”, but our long-term goal is to provide continuous measurements which will be used to create spatial flow maps (Figure 1). Such maps are ultimately needed for evaluating the spatial distribution of flow patterns in global coordinates.

II. BACKGROUND

Existing flow measurement techniques – Several methods of flow measurement capable of delivering estimates for the flow primitives, bulk flow velocity and bulk flow angle, have been developed. The most common techniques are hot-wire anemometry [23], laser Doppler velocimetry [40], acoustic Doppler velocimetry [26], and particle image velocimetry [32].

Acoustic Doppler velocimetry (ADV) [24] has become a common technology for flow measurements under both field and laboratory conditions which is straightforward to set-up and operate. ADV devices are based on the Doppler shift principle which uses two or more acoustic pulses of different duration at different time intervals. The back-scattered energy in a sampling volume is recorded after each pulse. The velocity is calculated as a function of the phase difference between returned signals. This technique can provide individual measurements of all three velocity components, the strength of the velocity fluctuations, and temporal correlation between the directional components. Several commercial ADV devices are available for field measurements in rivers, lakes, and for maritime applications. Considering measurements in rivers, ADV measurements can suffer from limited temporal resolution (typical is 1 Hz) and high signal-to-noise-ratios particularly for fast-moving unsteady flows with turbulence and air entrainment [15], [28]. Such conditions are typical for flow around hydraulic structures and in such cases the ADV spike noise can be confused with presence of turbulent components, complicating the analysis and interpretation of ADV measurements.

Laser Doppler velocimetry (LDV) [3] is based on the transmission of two beams of coherent laser light which are reflected by particles contained in the flow. The receiving optics record the return signal from which the velocity is estimated. The main advantages of the LDV include non-intrusive measurement, directional sensitivity, and the lack of calibration. The limitation of the method is irregular temporal sampling and the difficulty in measuring the velocities in close to wall-conditions where the optical path of the beams can change [31]. Furthermore, LDV systems cannot easily be

incorporated in field studies, and are only suitable to measure complex flows under sufficiently controlled conditions.

The principle of particle image velocimetry (PIV) [45] is based on the analysis of a recorded sequence of images taken as particles move within in a volume of fluid illuminated by a laser light source. The implementation of PIV is largely dependent on the choice of the system components, especially the choice of the light source and speed and resolution of the camera. This method has proven to be useful in laboratory conditions allowing for the measurement of entire flow structures and the determination of turbulence parameters [25]. The sequence of recorded images provides a series of spatial velocity distributions, whereas ADV or LDV systems return only point-based measurements of the flow velocity. The PIV technique demonstrates high accuracy in flow measurements however it suffers from practical limitations for use in field experiments where the necessary equipment cannot be easily installed [6]. Furthermore, as a passive measuring technique, the PVI method provides the spatial extent of the hydrodynamic interactions, but cannot directly measure how flows are experienced by the submerged object itself.

Thermal flow sensors [19] consist of electrically heated wire or film which are maintained at constant temperature. When the wire or the film is exposed to fluid flow, it rapidly cools and rate of heat loss can be correlated to the fluid flow velocity. The flow velocity measurements using thermal sensors are strongly affected by the fluid temperature, requiring temperature correction or compensation by the measuring system [23]. In some cases, the sensor has to be preheated to a temperatures higher than the fluid temperature which is not practically always possible. Similarly to ADV systems, commercially available thermal flow sensors are currently not suitable for field measurements around hydraulic structures due to the fragile sensor heads and the uncertainty caused by high-amplitude fluctuations in the flow field.

Although commercial devices exist using the above listed technologies, their usage remains largely confined to laboratory flow studies. The only technology suitable for field conditions around hydraulic structures, ADV, often suffers from a lack of temporal resolution and problems with spiking when measuring natural flows with air entrainment. LDV and PIV require extensive measurement setup and are generally impractical for field studies. Thermal sensors may require intensive calibration, contain fragile components, and are sensitive to large local fluctuations in the flow field. In this work, it was important that the developed sensor array would be accurate and robust enough to withstand field conditions, could be mounted inside fish-shaped probe body, and require as little calibration as possible while still delivering reliable measurements in challenging flow conditions. In order to achieve this, we use piezo-resistive pressure sensors which can be mounted in an array replicating a fish’s lateral line [43]. The piezo-resistive sensors used in this work are inexpensive, demonstrate high sensitivity, and exhibit sufficient linearity over an expected operational temperature range of $0 - 30^{\circ}\text{C}$. Thus the sensors are robust enough to be used in a wide range of field experiments. It should be noted that the one drawback to using piezoresistive sensors is that they often suffer from

sensor drift, and a discussion on drift compensation is provided in Section IV.

Artificial fish lateral line probe – Although most fish species perceive their spatial environment through vision, the lateral line has been long recognized as playing a key role in flow sensing capabilities [29], [42]. The lateral line response is used for orientation within turbulent currents [22], prey tracking, schooling, and possibly monitoring self-motion [11]. The lateral line system provides information contained in both local (particle motion) and distant (sound pressure) signals. The lateral line itself consists of a discrete set of receptors, called neuromasts which are distributed over the fish's body and provide information about changes in the local and global flow conditions.

The lateral line's unique properties allow for high-fidelity underwater perception and navigation and have motivated scientists to construct artificial organs mimicking the fish lateral line sensing system [16], [33], [17], [20], [21]. Several versions of flow sensing arrays located on the sides of a fish-shaped robot or sensor have been proposed [38] using piezoresistive sensors as well as with capacitive, piezoelectric, and magnetic sensors. In this work, we utilize an array of commercially available piezoresistive sensors. The sensors measure the strain on a silicon diaphragm whose electrical response is directly proportional to the dynamic pressure experienced by the sensor body. Such devices, if broadly implemented could facilitate expanding the functionality of underwater robots, even allowing them to reconstruct hydrodynamic images of complex underwater environments (Figure 1).

Growing interest has been exhibited in the study of how flow-based detection can be implemented using an artificial lateral line [11], [47]. Research in the field has now evolved from proof-of-concept to practical results, albeit under laboratory settings. In [43] pressure readings are used to differentiate between steady and unsteady flows, determine the orientation of the robot with respect to the flow, and compute the features of periodic turbulence under laboratory conditions. In [36] the authors show that the detection of flow regimes, robot orientation with respect to flow, flow speed, and the position of the robot in a wake of an object, focusing on the applications relevant to underwater robot control. In [8] the authors provide a transition metric between steady and unsteady flows based on the pressure difference between the anterior and side sensors. They also show that the vortex shedding frequency and magnitude can be used to detect the eddy size and flow speed. Jung et al. [18] demonstrate that flow-aided path following for an underwater robot is a more effective strategy than when robot is not capable of sensing the flow. Akanyeti et al. [2] study what features can be detected in periodic turbulence using a lateral line probe. In the recent work by Ristroph et al. [35] it is also shown that pressure sensors can be leveraged as components of an artificial lateral line and it is demonstrated that the signal response changes according to the physical flow parameters, experimentally showing how the pressure-sensing system of a fish is concentrated mainly near the head. In a recent work by De Vries et al. [14], flow parameters were estimated based on potential flow theory (assuming an ideal, irrotational flow), modeling the fluid flow passing a

symmetric foil. The information from all lateral line sensors is combined to provide measurements using recursive Bayesian filtering. Such an approach could be difficult to implement for a complex fish-shaped body, especially considering turbulent flow conditions. Thus recent research works demonstrate that flow sensing arrays or artificial lateral line probes are suitable for detection of physical flow descriptors. The lateral line probe commonly consists of multiple, synchronous sensors. Thus either single sensors can be selected from the sensing array or data fusion of multiple sensors can be used for flow parameter detection. Many previous works demonstrate results using higher level features (e.g. frequency components) without considering any direct physical interpretation. Our work is based on primitive hydrodynamic features with clear physical meaning and are also robust to the types of noise and signal distortion expected in natural environments.

Contributions – The contributions of our work can be summarized as follows:

- We propose a bio-inspired sensor probe consisting of an artificial lateral line sensor array for in-situ measurements of complex natural flow patterns (e.g. for the evaluation hydraulic structures in a river) and introduce the bulk flow velocity and flow angle as the chosen pattern primitives.
- We introduce a ridge regression based bulk flow angle and bulk flow velocity estimation methods using the raw (calibrated) multi-dimensional sensor readings that correlate with the physical quantity of dynamic pressure.
- We introduce a joint estimation signal processing pipeline that consists of the above regressors, and by augmenting them with a computational transformation to a pose invariant “canonical pose” our system recovers the flow angle and velocity from signals measured in arbitrary pose.
- We propose a generic calibration procedure for pressure sensing artificial lateral line arrays which includes corrections for temperature, atmospheric pressure, water depth, and sensor bias.
- We experimentally evaluate the limits, accuracy, and robustness (with respect to orientation misalignment) of the probe with measurements using independent data for training, validation, and testing.

III. SENSOR PROBE AND DATA ACQUISITION

The artificial lateral line consists of 16 piezoresistive pressure sensors (SM5420C-030-A-P-S, Silicon Microstructures) mounted on a fish-shape sensor probe, for hardware details see [39]), and two accelerometers (ADXL325BCPZ, Analog Devices). The pressure sensors have a full sensitivity over a 0-206842.72 Pa span. The signals undergo first and second stage amplification (AD8656ARMZ, Analog Devices) and are then digitized with a 16-bit analog to digital converter (AD768BSPZ, Analog Devices) Temperature estimates via current consumption are made using a shunt resistor. The output signals are 10x oversampled and transmitted over a serial connection at a 250 Hz sample rate. Five of the sensors (sensors 2, 5, 8, 11 and 14) located on the bottom are non-parallel to the primary lateral line and therefore a total of 11

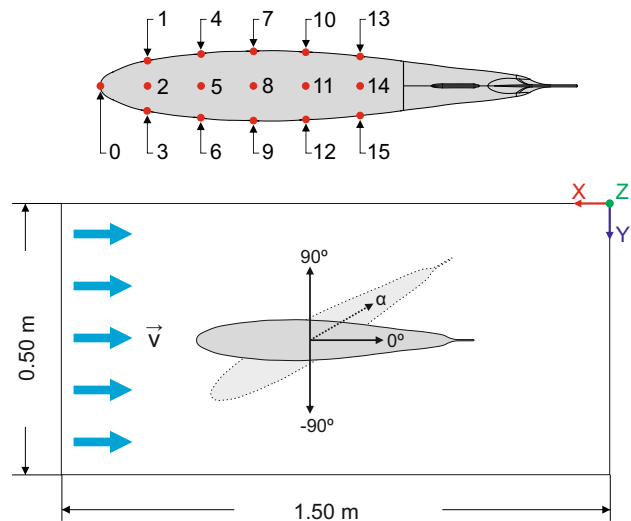


Figure 2: The artificial lateral line probe: the closeup image (bottom left) shows the open electronics bay, the cables are fed through the stainless steel mounting pole. Location of the 11 lateral line piezoresistive pressure sensors (top right) and the set-up used in the experiments.

(nose plus 5 on each side) sensors (0, 1, 3, 4, 6, 7, 9, 10, 12, 13, and 15,) are used in our experiments. The sensor platform and sensor locations are shown in Figure 2.

The piezoresistive pressure sensor produces a current response whose signal is amplified and converted using a 16-bit ADC. From each of the 16 sensors ($ps0 - ps15$) the following signal values are stored (Figure 3): 1) sensor current consumption ($v1$), 2) first stage amplified pressure ($v2$), 3) offsets subtracted from the second amplification stage output to fit to 16-bit conversion ($v3$) and 4) second stage amplified pressure ($v4$). In our preliminary experiments we found that the second stage amplification is not necessary for the estimation of flow primitives and therefore used the first stage signal ($v2$) as the pressure measurement $s(t)$ in all reported experiments.

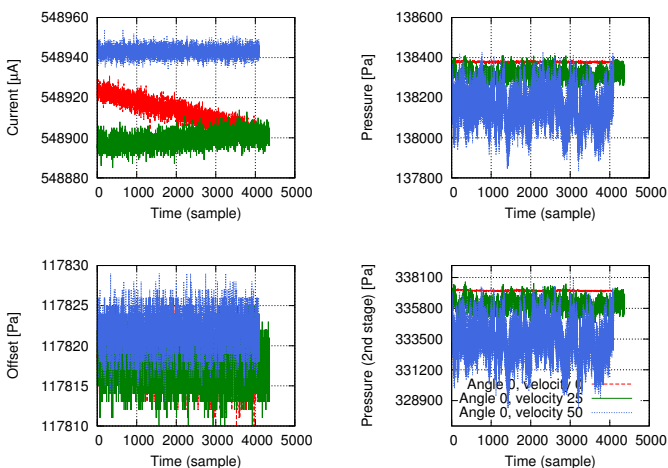


Figure 3: The $ps0$ (nose) pressure sensor readings for the perpendicular (0°) bulk flow velocities $V = 0, 25, 50$ cm/s.

The true sampling frequency of the lateral line probe was verified and the effective sampling frequency varied from 122 to 128 samples per second (Hz) with an average of 125.0 and median 126. When mapping the discrete sample frequencies to true frequencies the average sampling frequency $f_s = 1/125 = 125\text{Hz}$ is used.

IV. CALIBRATION AND NORMALIZATION

Our lateral line sensor is sensitive to fluctuations in all of the hydrodynamic variables (velocity, vorticity, pressure) which is evident from our laboratory experiments where the artificially generated flow velocity varied between 0 to 50cm/s (0.5m/s). This range was chosen as it encompasses the bounds of the rheotactic threshold for fish. Rheotaxis is the spontaneous self-orientation of a body against the bulk flow direction, which occurs only after a minimum flow velocity has been achieved. Fish are grouped according to the threshold velocities required to initiate rheotaxis [1], where an accuracy of 10cm/s is sufficient to cover typical indicator species. The major downside of the high sensitivity of our device is that accurate calibration is required in order to make measurements between different experiments comparable. Without the calibration, raw measurements between experiments following the same setup may vary significantly (Figure 5). Our step-wise calibration procedure is shown in Figure 4 for a single experiment.

Temperature normalization – Temperature dependent outputs are common to many electric devices, and the pressure readings of the lateral line sensors are influenced by the device's internal temperature. Further complications arise when considering the rapid and unsteady heat transfer between the sensor body and surrounding turbulent flow. Piezoresistive sensors have coefficients which vary inversely with the temperature, and a variety of methods have been developed for temperature normalization; self-temperature compensation,

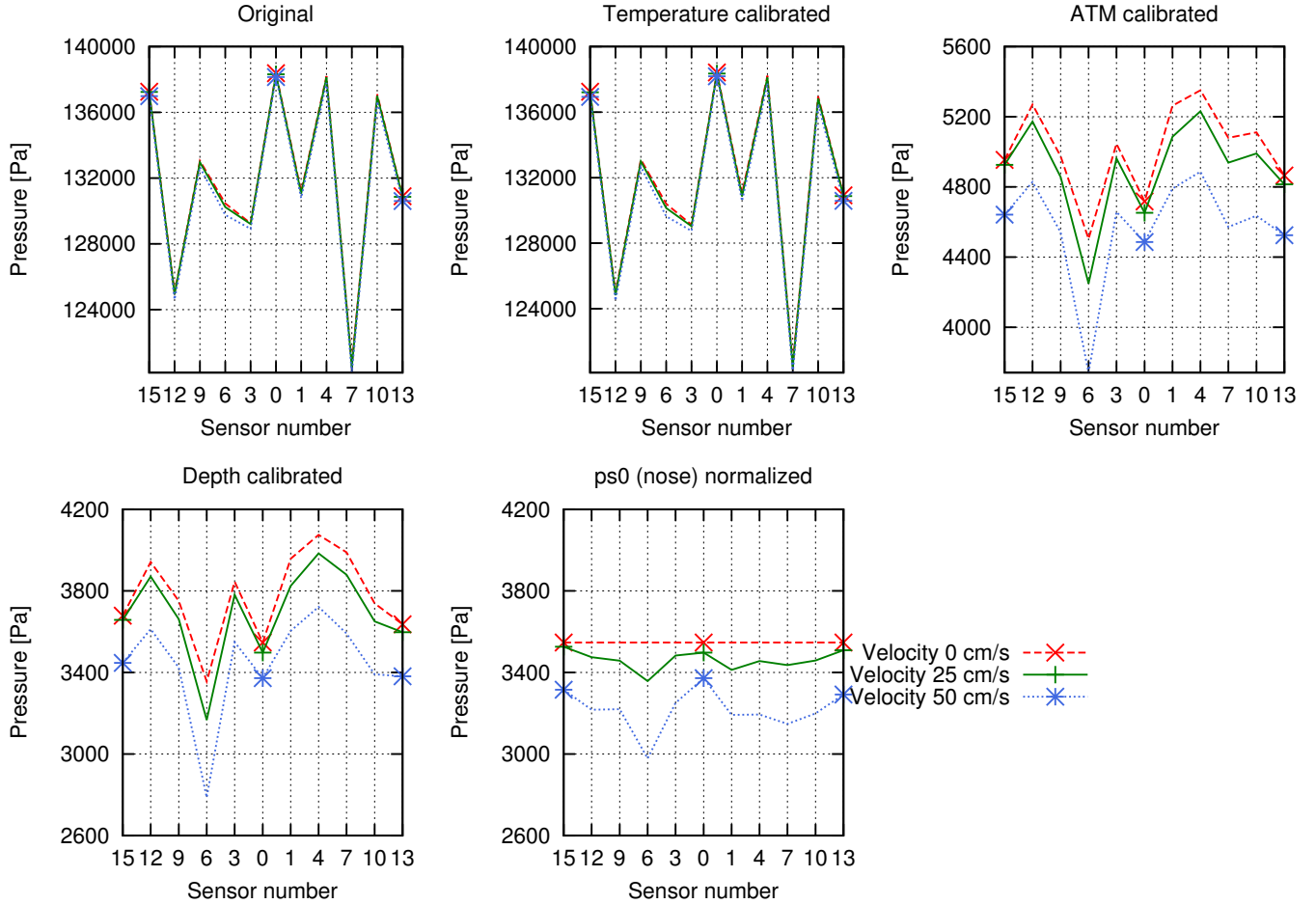


Figure 4: The discrete calibration and normalization steps (from left to right) (E2).

span compensation using series and parallel resistive elements, multiplier circuits, and complex solutions using a network of laser trimming resistors, and digital systems outfitted with micro controllers [12], [46]. Due to the measurement system already having digital outputs, in this work we opted for a software-based temperature calibration workflow. The temperature calibration was carried out using known measurements at fixed flow velocities after the working temperature had stabilized (after a warm-up period in water). Static water conditions ($v = 0\text{ cm/s}$) were also used for calibration in the experiments. We then applied a linear calibration model for which the temperature difference defines the additive bias term:

$$s_{T_M}(t) = s_{T_C}(t) + \beta_1 \Delta T = s_{T_C}(t) + \beta_1 (T_M - T_C) \quad (1)$$

where T_M is the device temperature during the measurement and T_C during the calibration and β_1 is the calibration constant (the slope of the linear correspondence function) in the $\text{Pa}/^\circ\text{C}$ units.

Our device is not equipped with an internal thermometer, but for slow flow speeds the circuit current consumption $c(t)$ (top left in Figure 3) provides a linear proxy to temperature, providing a dynamic temperature calibration using the current

measurements¹:

$$\begin{aligned} s_{T_M}(t) &= s_{T_C}(t) + \beta_1 \Delta T \approx \\ &\approx s_{T_C}(t) + \beta_1 \Delta c = \\ &= s_{T_C}(t) + \beta_c (c_M(t) - c_C(t)) . \end{aligned} \quad (2)$$

The water temperature in our experiments was $T_C = 20^\circ \pm 3^\circ$. In (2) the calibration constant β_c unit is Pa/A . For multiple lateral line sensors ($D = 11$ for the sensor array used here), the constant is actually a vector constant $\beta_c = (\beta_c^1, \beta_c^2, \dots, \beta_c^D)^T$ representing different constants for different sensors.

Atmospheric pressure calibration – For convenience, we remove the atmospheric pressure effect from the temperature corrected signal. In cases where knowledge of the atmospheric pressure is necessary, more involved pressure calibration such as the use of pressure chambers may be required [13]. During our calibration routine, the atmospheric pressure is measured at the same calibration temperature ($T_C = 20^\circ\text{C}$ in our case) and is applied separately to different pressure sensors (ATM calibration vector). For notational simplicity we use $s(t)$ to

¹Note that the assumption has only been verified over the range of slower flow speeds used in our experiments

denote also the calibrated pressure signal. In the calibration formula

$$\mathbf{s}(t) = \mathbf{s}_{T_C}(t) - \mathbf{s}_{T_C, P_{ATM}}(t) \quad (3)$$

$\mathbf{s}_{T_C, P_{ATM}}(t)$ denotes the (average) measurement made in the atmospheric pressure in indoors air temperature.

Depth calibration – Our calibration workflow for pressure first accounts for the effect of atmospheric pressure using a calibrated offset. Another important factor influencing the pressure reading is the flow depth, as it makes up the majority of the total pressure, and has an especially large contribution at slower flow velocities. In order to measure flow velocities invariant to the depth we need to apply the depth correction constant β_2 ($D \times 1$ vector). The real pressure (independent of depth) was computed according to the equation

$$\mathbf{s}(t) = \beta_2 \mathbf{I} \mathbf{s}(t) \quad (4)$$

where the constant β_2 was measured using the same calibration flow velocity and temperature (\mathbf{I} is the identity matrix). More advanced methods for pressure sensor calibration such as support vector machines or neural networks can also be applied [44], [49]. It was found that the obtained accuracy of our atmospheric pressure and depth calibration workflow did not warrant the use of more complex methods.

Sensor bias normalization – During measurement, the lateral line probe can be considered as a synchronized sensor array. However, the measurements may suffer from offset and scale biases and do not have consistent target data due to the influence of environmental changes. Furthermore, the observed pressure readings between devices can vary depending on the selected components in the circuit (e.g., the ADC) and to remove these effects from the individual pressure sensors it was necessary to apply sensor bias normalization.

Ideally, in the no-flow conditions all sensors should exhibit identical performance. We can computationally enforce this by measuring the responses at a single depth or over multiple depths, including temperature calibration under static (no flow) conditions, and normalize all sensor readings to a single, mean or median of all sensors. In our case, we normalize all readings by the nose sensor (ps_0):

$$\mathbf{s}(t) = \mathbf{s}(t) - (\mathbf{s}(t) - s_{ps_0, T_C}(t)) \quad (5)$$

where s_{ps_0, T_C} is the “sensor baseline pressure”.

V. METHODS

A. Basic notation

The lateral aquatic pressure signal is D -dimensional ($D = 11$ in this work) temporal vector $\mathbf{s}(t)$ where the discrete time instants $t = 0, 1, \dots, N$ correspond to samples taken with the 125Hz sampling rate. The sampling window is $1/125\text{s} = 0.008\text{s} = 8\text{ms}$. A single pressure reading from the artificial lateral line sensor is a vector

$$\mathbf{s}(t) = \begin{pmatrix} s_0(t) \\ s_1(t) \\ \vdots \\ s_{Dt}(t) \end{pmatrix} \quad (6)$$

and signal processing and detection is based on temporal data where the consequent sample vectors are concatenated to a sample matrix

$$\mathbf{S}_{t_0} = \begin{pmatrix} \mathbf{s}(t_0 + 0) & \mathbf{s}(t_0 + 1) & \cdots & \mathbf{s}(t_0 + T - 1) \\ s_0(t_0 + 0) & s_0(t_0 + 1) & \cdots & s_0(t_0 + T - 1) \\ s_1(t_0 + 0) & s_1(t_0 + 1) & \cdots & s_1(t_0 + T - 1) \\ \vdots & \vdots & \ddots & \vdots \\ s_{Dt_0 + 0} & s_{Dt_0 + 1} & \cdots & s_{Dt_0 + T - 1} \end{pmatrix} \quad (7)$$

of T samples. Our goal is to process the sample matrices in spatially distinct locations, with arbitrary orientation of the sensor to produce a spatial mapping of global flow pattern primitives (see Figure 1).

B. Physical model

The signal samples $s_i(t)$ in (6) directly measure the total energy of the system which consists of the fluid kinetic energy per unit mass, $\frac{v^2}{2}$ and hydraulic head, $h + \frac{pg}{\rho}$ which follows the Bernoulli law for conservation of energy [41]

$$\frac{v^2}{2} + h + \frac{pg}{\rho} = s_0, \quad (8)$$

where g is the acceleration due to gravity, h is the geodetic height of the measurement point, ρ is the density of the fluid, and s_0 represents the constant total energy experienced at the stagnation point. At the stagnation point the fluid velocity is brought to zero and all kinetic energy is converted into pressure energy. In our case the nose sensor s_0 is a true stagnation point only when the body is oriented with zero angle into the flow. Thus the nose sensor serves as a hydrodynamic datum only when the body is correctly oriented. The side sensors are not ideal hydraulic head sensors due to the flow around the body, which creates an additional kinetic contribution at each location. This equation suggests that when held at a fixed location where ρ and h are constant the pressure difference across the nose and side sensors should increase quadratically as a function of the flow velocity:

$$(s_0 - s_i) = \frac{\rho v^2}{2} \quad (9)$$

We compare the theoretical and experimental results in Figure 5 where it can be seen that there is a systematic underestimation of velocity. This is expected due to the additional contribution of the dynamic pressure on the side sensors which reduces the total pressure difference. Since the geodetic height and fluid density are fixed, the difference must be due to the influence of kinetic energy at the non-ideal side sensors. The full theoretical derivation and additional discussion on lateral line velocity estimation can be found in [36].

C. Low level features

As shown in the previous section, changes in the bulk flow velocity $v(t)$ are directly reflected as changes in the pressure measurements $\mathbf{s}(t)$ as predicted by the Bernoulli law in Eq. 9 and in Figure 5 this was illustrated using average pressure measurements in our experiments. These findings provide

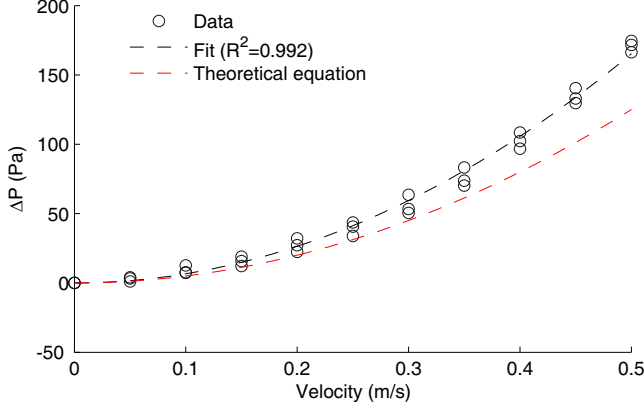


Figure 5: Pressure estimates for different velocities: experimental versus theoretical results.

additional motivation to directly apply the flow primitives $s(t)$ as the low level features since they have direct physical meaning.

A single sample reading from one sensor is too noisy due to its short duration, and more robust features can be constructed by substituting by the expected value

$$\mathbf{x} = \int_{-\infty}^{+\infty} s f(s) \quad (10)$$

where $f(\cdot)$ is the probability density function (pdf) of s and which in the discrete case is identical to the signal average:

$$\mathbf{x} = \frac{1}{T} \sum_{i=0}^{T-1} s(i) \quad (11)$$

over T discrete samples. A suitable time duration T for averaging is analyzed in our experiments. While (11) corresponds to the first order statistics we also evaluate the second order statistics

$$\mathbf{x} = \frac{1}{T-1} \sum_{i=0}^{T-1} (s(i) - \mu_x)^2 \quad (12)$$

where μ_x is the average computed by (11) or in the case of more robust rank-order statistics $\mu_x = \text{median}(\{\mathbf{x}\}_L)$.

D. Kernel ridge regression

Kernel ridge regression [37] provides an effective and flexible tool for regression and is computationally inexpensive thanks to the kernel trick which performs complex feature mappings by dot products. Kernel ridge regression has also gained significant momentum in the vision community due to superior results in many challenging vision regression applications [4], [9], [10].

The classical way of solving regression problems is the ordinary least squares (OLS) which minimizes the squared loss:

$$\sum_i (y_i - \mathbf{w}^T \mathbf{x}_i)^2 \quad (13)$$

However, due to a limited number of training examples, the variance of the linear regression parameters \mathbf{w} by OLS can be large which reflects unreliable regression (over-fitting) between the co-variables \mathbf{x}_i (our low level features) and the response variables y_i (the bulk flow angle or velocity or both in our experiments). An effective way to overcome this problem is to penalize the norm of \mathbf{w} as in ridge regression. Instead of minimizing squared errors, ridge regression minimizes the following cost:

$$J(\mathbf{w}) = \sum_i (y_i - \mathbf{w}^T \mathbf{x}_i)^2 + \lambda \|\mathbf{w}\| \quad (14)$$

where λ is the positive regularization parameter that reduces the estimate \mathbf{w} variance at the expense of increasing training errors (the trade-off between the bias and variance). In practice, one can use cross-validation [30] to find the optimal regularization parameter that minimizes the cross-validation errors.

Saunders et al. [37] derived a dot product form for the predicted target value of a novel input \mathbf{x} , i.e. $\mathbf{w}^T \mathbf{x}$:

$$\mathbf{y}^T (\mathbf{K} + \lambda \mathbf{I})^{-1} \boldsymbol{\kappa} \quad (15)$$

where \mathbf{K} is the training set dot product matrix

$$\mathbf{K}_{i,j} = \mathbf{x}_i^T \mathbf{x}_j \text{ for } i = 1, 2, \dots, N \text{ and } j = 1, 2, \dots, N, \quad (16)$$

for a training set of N examples and $\boldsymbol{\kappa}$ is the prediction dot product vector

$$\boldsymbol{\kappa}_i = \mathbf{x}_i^T \mathbf{x} \text{ for } i = 1, 2, \dots, N. \quad (17)$$

The formulation in (15) contains the training and new example feature vectors in the dot product forms in (16) and (17) and therefore the kernel trick can be readily applied [37]. The formulation turns the ridge regression (RR) in (14) to kernel ridge regression (KRR) where the original features \mathbf{x} can be replaced with kernel feature transformation $\mathbf{x}_i \rightarrow \Phi(\mathbf{x}_i)$. The regression is particularly efficient when solving in the dual space if the transformation is induced by a dot product kernel $k(\mathbf{x}_i, \mathbf{x}_j) = \Phi(\mathbf{x}_i)^T \Phi(\mathbf{x}_j)$ where $k(\cdot)$ is the kernel function. In this work, we experiment with the polynomial kernels $k(\mathbf{x}_i, \mathbf{x}_j) = (\mathbf{x}_i^T \mathbf{x}_j + 1)^d$ and use three-fold cross-validation.

E. Multivariate kernel ridge regression

A multivariate extension to kernel ridge regression was presented by An et al. [4] for the multivariate ridge regression:

$$J(\mathbf{W}) = \sum_i \|\mathbf{y}_i - \mathbf{W}^T \mathbf{x}_i\|^2 + \lambda \|\mathbf{W}\|^2 \quad (18)$$

Note that now the response variable \mathbf{y} is a vector and the regression weights form a matrix \mathbf{W} . We can establish the multivariate form similar to (15):

$$\mathbf{W}^T \Phi(\mathbf{x}) = \mathbf{Y} (\mathbf{K} + \lambda \mathbf{I})^{-1} \Phi^T(\mathbf{x}) \Phi(\mathbf{x}) = \mathbf{Y} (\mathbf{K} + \lambda \mathbf{I})^{-1} \boldsymbol{\kappa}(\mathbf{x}) \quad (19)$$

where $\boldsymbol{\kappa}(\mathbf{x}) = [k(\mathbf{x}_1, \mathbf{x}) \ k(\mathbf{x}_2, \mathbf{x}) \ \dots \ k(\mathbf{x}_n, \mathbf{x})]^T$. This form again avoids access the feature vectors as long as the kernel function $k(\cdot)$ exists.

VI. EXPERIMENTS

Some of the most important flow primitives relevant to multiple applications such as flow measurement, underwater robotics, and fish biology are those used for the automated alignment of the swimming body with the bulk flow. This requires joint estimation of the bulk flow velocity and angle with respect to the probe coordinate system (ego-centric). In nature the joint-estimation of the velocity and angle allows for rheotaxis, where a fish turns to face toward oncoming current (bulk flow). In the following experiments we investigate methods for the detection of the hydrodynamic primitives required for the alignment: 1) bulk flow angle, 2) bulk flow velocity, and 3) joint detection of angle and velocity.

A. Data

The experiments were performed in a flow tunnel with a working area of $150 \times 50 \times 50 \text{ cm}$ (see Figure 2). Diffusers in front of the working section were used to generate a steady turbulent flow. The sensor probe was mounted on a platform installed in the flow channel working section. For angle and flow speed measurements, the sensor was rotated in the X-Y plane while keeping the depth constant. Due to the experimental setup, small depth variations in the flow tank occur between different experiments. The initial pose configuration was the sensor mounted such that it was facing the core flow corresponding to 0° rotation.

All measurements within each experiment were carried out over a one-day period starting from still water conditions in the tank. To ensure viable ensemble averages, the motor was allowed to warm up to the working temperature before measurements were acquired (Section IV). The details of the different experiments are provided in Table I.

Table I: Measurements carried out for the *Tallinn Nov 2014* data set.

E2	Angles: $0^\circ, \pm 15^\circ, \pm 30^\circ, \pm 45^\circ, \pm 60^\circ, \pm 75^\circ, \pm 80^\circ, \pm 90^\circ$ Velocities: 0, 5, 10, 15, 20, 25, 30, 35, 40, 45, 50 cm/s
E2a	Angles: 0° Velocities: 0, 5, 10, 15, 20, 25, 30, 35, 40, 45, 50 cm/s
E2b	Angles: 0° Velocities: 0, 5, 10, 15, 20, 25, 30, 35, 40, 45, 50 cm/s
E2c	Angles: 0° Velocities: 0, 5, 10, 15, 20, 25, 30, 35, 40, 45, 50 cm/s
E5	Angles: $0^\circ, \pm 15^\circ, \pm 30^\circ, \pm 45^\circ, \pm 60^\circ, \pm 75^\circ, \pm 80^\circ, \pm 90^\circ$ Velocities: 0, 5, 10, 15, 20, 25, 30, 35, 40, 45, 50 cm/s

B. Hydrodynamic primitive 1: Bulk flow velocity

For the first experiment we applied the kernel ridge regression with the quadratic polynomial kernel $k(\mathbf{x}_i, \mathbf{x}_j) = (\mathbf{x}_i^T \mathbf{x}_j + 1)^2$ ($d = 2$). For the low level features in Section V-C we tested the averaging intervals $1 \dots 25 \text{ s}$ ($T = 125 \dots 3125$ samples). The standard calibration procedure from Section IV using the no-flow measurements of the training set was applied.

We performed experiment two times. First time we used *E2* as evaluation test and *E5*, *E2a*, *E2b*, and *E2c* for training (only one at a time). Second time we used *E5* for testing and *E2*, *E2a*, *E2b*, and *E2c* for training. In both cases we used bootstrapping. As the performance measure we report the mean absolute error in velocity

$$\epsilon_v = \frac{1}{N} \sum |v - \hat{v}| \quad (20)$$

where N is the number of test samples.

The results for the velocity experiment are presented in Table II and Figure 6. We can make the following three observations based on the results. Despite the careful calibration, there are significant differences between the data sets which are partly due to temporal variations in the dynamic pressure field between them. This is due to the presence of fully turbulent flow, which cannot be replicated exactly even when the experimental conditions are held constant. The observed variations between experiments makes the signal mean feature, the first-order moment, too sensitive for robust velocity estimation and unlikely to perform well in field conditions. However, the second-order moment, the signal variance, does provide robust and accurate velocity estimates even for the extrema angles $\pm 90^\circ$ for which the average error is below $\pm 6.5 \text{ cm/s}$. This is because the statistical properties of a steady turbulent flow become similar when time averaging is performed [5]. The effect of the signal variance computing period can be seen in Figure 6 (bottom) where the results improve until convergence at approximately 5 seconds. The main result is that the velocity estimation of slow turbulent velocities can be robustly and accurately estimated with the sensor probe by pointing the sensor approximately into the bulk flow and using signal variance computed over 5 s period and with a quadratic regression model. The final observation is that the error distribution is not symmetric when considering right or left rotations. This is especially apparent for large angular deviations $> \pm 45^\circ$, where it can be seen that large angular deviations to the left cause larger errors than to the right. The asymmetry of the pressure field signal at large angles is a result of the superposition of small differences in the individual pressure sensors, the body geometry, and the dynamic response (bending and vibrating) of the probe's body. Thus our probe exhibits a tendency for right-handed "lateralization" at large angular deviations.

Table II: The experiment *E2* velocity estimation errors for using different data sets in training (the *E2* row represents the training set error).

	0°	$\pm 15^\circ$	$\pm 30^\circ$	$\pm 45^\circ$	$\pm 60^\circ$	$\pm 90^\circ$
Signal average feature						
E2	2	25	51	94	159	163
E2a	60	19	23	39	64	61
E2b	15	28	36	66	117	125
E5	709	495	328	206	253	94
Signal variance feature						
E2	3.9	4.3	5.6	6.0	5.1	7.0
E2a	3.8	4.1	5.2	5.2	5.0	5.2
E2b	4.2	4.2	5.3	5.3	5.0	5.4
E5	3.9	4.1	5.4	5.6	5.8	5.9

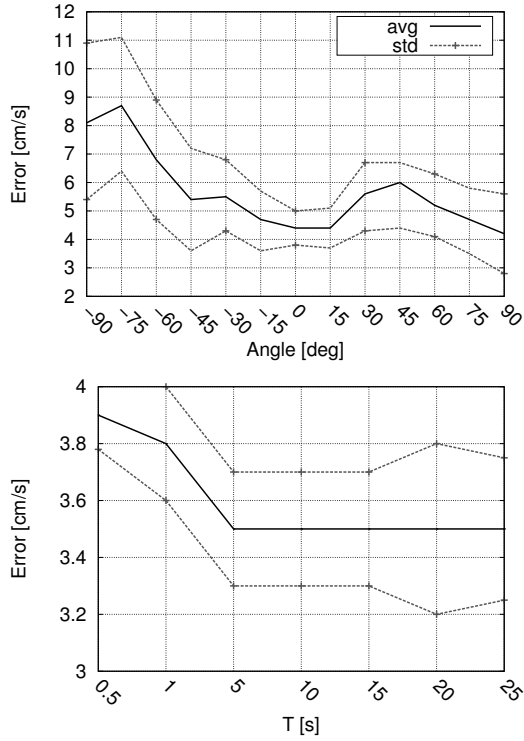


Figure 6: Average bulk flow velocity estimation error and standard deviations over all experiments including probe misalignment with the bulk flow (variance feature). Top: error as the function of the misalignment angle ($T = 10$ s). Bottom: effect of the feature averaging duration (T).

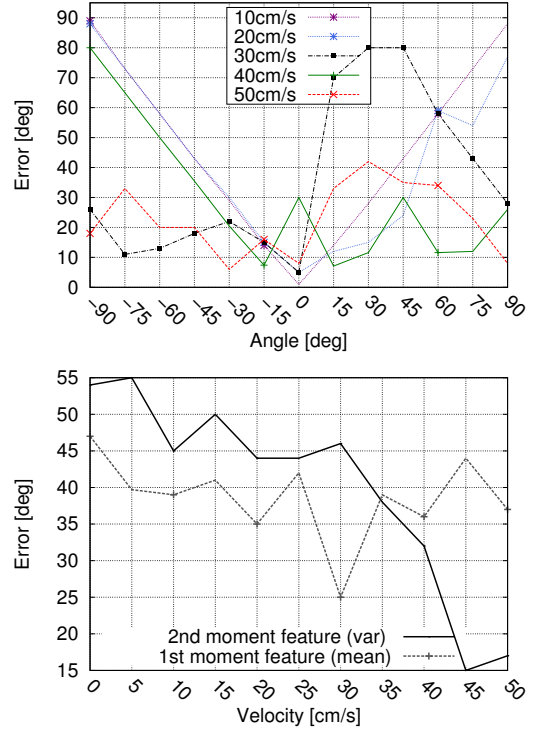


Figure 7: Bulk flow angle estimation error ($E2$ for training and $E5$ for testing). Top: angular errors for different velocities, result of a single experiment. Bottom: total average error over all angles and experiments as a function of flow velocity.

C. Primitive 2: Bulk flow angle

For the angle estimation the first order polynomial kernel ($d = 1$) provided the best results. It is worth noting that while the velocity estimation performed well even with a single sensor (e.g., s_0 - “nose”) the angle estimation completely fails for a single sensor and improves rapidly as the number of sensors increase. This finding indicates the importance of leveraging the full array of lateral line sensors. Here we report absolute errors using the estimated angle (in degrees) as the performance measure.

In this experiment, we used the two independent sets of angle and velocity measurements: $E2$ and $E5$. The angle estimation errors shown in Figure 7. In the top graph in Figure 7 it is evident that the angle estimation error improves for increased velocities and errors are somehow tolerable for the highest velocities (> 40 cm/s) for which the average estimation error is below 20° . The performance collapse for velocities below the limit is rather striking and it seems that the angle estimation is unreliable below the limit (see the bottom graph in Figure 7). The mean feature performs favorably to the variance feature on lower velocities, but again suffers from the sensor depth variation between the experiment sets.

D. Primitive 3: Joint estimation of flow angle and velocity

For the joint detection of bulk flow velocity and angle the multivariate form in (18) (Section V-E) may be applied,

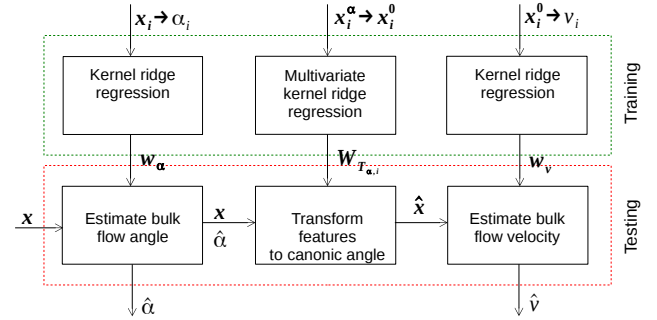


Figure 8: Step-wise framework for joint bulk flow velocity and angle estimation. The first step estimates the angle ($\hat{\alpha}$), the second step transforms responses to the canonical space by the estimated angle and the corresponding multivariate transformation T_{α_i} . The final step estimates the flow velocity using the transformed features \hat{x} .

but since this requires a rather large training set we break the problem in three stages illustrated in Figure 8. The stages 1 (estimate bulk flow angle) and 3 (estimate bulk flow velocity) have already been investigated in the previous experiments. However, the velocity estimate degrades with increasing deviation from bulk flow (0° , see Figure 6). This can be improved if the angle of rotation α is known a priori, but this is a largely invalid assumption in practice and therefore

we propose a canonical transformation T_α which transform responses measured at the angle α to the angle 0° denoting it as the canonical space. A discrete set of transformations can be precomputed using the multivariate kernel regression and for novel measurements the estimated angle $\hat{\alpha}$ of stage 1 is used to select the closest canonical transformation.

We computed the canonical transformation from the E5 data set. As a training set for angle estimation the data set E2 was used. For training and testing of velocity estimation we used the same scheme as in Section VI-B. The results shown in Figure 9 clearly indicate that the largest benefit from the transformation is obtained when the sensor is significantly misaligned, i.e., greater than -45° , 45° . If the canonical transformation is applied, then the error of the velocity estimation does not increase significantly for rotated measurements, instead varying from 4 to 6 cm/s. These results were obtained by averaging estimates over the four independent data sets used in training. In order to determine how the angle estimation error affects the joint estimates we performed three experiments: no transformation, canonical transformation selected by the ground truth angle and canonical transformation selected by the estimated angle. The ground truth angle provides superior results, followed by the estimated angle. It was found that the joint estimation using the canonical method did not significantly decrease the overall error as compared to the non-canonical approach, but was effective in removing the asymmetry associated with large angular deviations. For this reason, the joint estimation pipeline is to be recommended over single-step estimates of the bulk flow velocity and angle (see Figure 9).

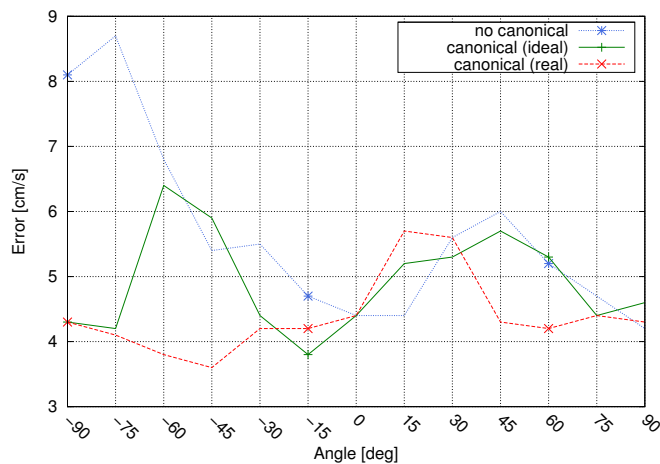


Figure 9: Results for the bulk flow velocity estimation from unknown angle with no angle transformation (“no canonical”), with ground truth angle (“canonical (ideal)”) and using the angle estimation pipeline in Figure 8 (“canonical (real)”).

VII. CONCLUSIONS

In this work we investigate the estimation of flow primitives with a new type of probe design consisting of an artificial lateral line array. The objective of this work was to introduce a pipeline including calibration and signal processing methods

to measure complex local flow parameters. In particular, we focused on practical methods for the estimation of the two key local flow primitives the bulk flow velocity and angle. The flow primitives can be used for establishing the required flow characteristics typical to hydraulic structures in order to identify the preferred hydrodynamic conditions for aquatic organisms. We formulated the flow pattern measurements as a signal regression problem and proposed kernel ridge regression as a suitable regression tool. Based on the results of laboratory experiments we made the following findings: a lateral line pressure sensor array can be an accurate and robust sensor probe for measuring bulk flow velocity, bulk flow angle as well as the joint estimation of both. For the studied velocities ($0 - 0.5m/s$), the signal variance computed over time period of $5s$ provides accurate flow velocity estimate. Using the same signal feature, the bulk flow angle can be estimated, but requires flow speeds $\geq 0.45m/s$. Furthermore, the joint estimation pipeline proposed in this work is capable of estimating the velocity and angle including large angular deviations from the ideal orientation, and removes the asymmetric error found at large angles. Using the framework outlined in Figure 8, a canonical transformation was developed which improves measurements for an arbitrary sensor pose, keeping the error across all angular deviations to $\leq 0.1m/s$. In future work we will use the sensor probe and signal processing pipeline to generate spatial maps of altered flows, using them for the quantitative evaluation of complex flows associated with hydraulic structures in a river. Moreover, we will investigate the possibility for continuous sensor self-calibration as a method to retrieve robust mean feature measurements.

REFERENCES

- [1] Beate Adam and Boris Lehmann. *Ethohydraulik*. Springer Berlin Heidelberg, Berlin, Heidelberg, 2011.
- [2] O. Akanyeti, R. Venturelli, F. Visentin, L. Chambers, W. M. Megill, and P. Fiorini. What information do karman streets offer to flow sensing? *Bioinspiration and Biomimetics*, 6:1748–3182, 2011.
- [3] H. E. Albrecht, N. Damaschke, M. Borys, and C. Tropea. *Laser Doppler and Phase Doppler Measurement Techniques*. New-York: Springer-Verlag, 2003.
- [4] S. An, W. Liu, and S. Venkatesh. Face recognition using kernel ridge regression. In *IEEE Conf. on Computer Vision and Pattern Recognition (CVPR)*, pages 1–7, 2007.
- [5] G. K. Batchelor. *The Theory of Homogeneous Turbulence*. Cambridge University Press, Cambridge ; New York, reprint edition, 1982.
- [6] L. Bertuccioli, G. I. Roth, J. Katz, and T. R. Osborn. A submersible particle image velocimetry for turbulence measurements in the bottom boundary layer. *Journal of Atmospheric and Oceanic Technology*, 19:1635–1646, 1999.
- [7] H. Bleckmann and R. Zelick. Lateral line system of fish. *Integrative Zoology*, 4:13–25, 2009.
- [8] L. D. Chambers, O. Akanyeti, R. Venturelli, J. Ježov, J. Brown, M. Kruusmaa, P. Fiorini, and W. M. Megill. A fish perspective: detecting flow features while moving using an artificial lateral line in steady and unsteady flow. *Journal of The Royal Society Interface*, 11, 2014.
- [9] K. Chen, S. Gong, T. Xiang, and C.C. Loy. Cumulative attribute space for age and crowd density estimation. In *IEEE Conf. on Computer Vision and Pattern Recognition (CVPR)*, pages 2467–2474, 2013.
- [10] K. Chen and J.-K. Kämäräinen. Learning to count with back-propagated information. In *The 22th International Conference on Pattern Recognition (ICPR2014)*, 2014.
- [11] S. Coombs. Smart skins: Information processing by lateral line flow sensors. *Autonomous Robots*, 11:255–261, 2001.
- [12] G. de Oliveira Coraucci, F. Fruett, and S. Finco. Silicon multi-stage current-mode piezoresistive pressure sensor with analog temperature compensation. In *IEEE Sensors*, pages 1526–1529, Oct 2011.

- [13] Z. D. Deng, J. Lu, M. J. Myjak, J. J. Martinez, C. Tian, S. J. Morris, T. J. Carlson, D. Zhou, and H. Hou. Design and implementation of a new autonomous sensor fish to support advanced hydropower development. *Review of Scientific Instruments*, 85, 2014.
- [14] L. DeVries, F. D. Lagor, H. Lei, X. Tan, and D. A. Paley. Distributed flow estimation and closed-loop control of an underwater vehicle with a multi-modal artificial lateral line. *Bioinspiration and Biomimetics*, 10(2), 2015.
- [15] D. E. Dombroski and J. P. Crimaldi. The accuracy of acoustic doppler velocimetry measurements in turbulent boundary layer flows over a smooth bed. *Limnology and Oceanography: Methods*, 5:23 – 33, 2007.
- [16] H. E. Daou, T. Salumae, A. Ristolainen, G. Toming, M. Listak, and M. Kruusmaa. A bio-mimetic design and control of a fish-like robot using compliant structures. In *Proceedings of the 15th International Conference on Advanced Robotics (ICAR)*, pages 563–568, 2011.
- [17] N. Izadi and G. J.M. Krijnen. Design and fabrication process for artificial lateral line sensors. In *Frontiers in Sensing: From Biology to Engineering*. Springer Verlag, 2011.
- [18] D.S. Jung, P.P. Pott, T. Salumae, and M. Kruusmaa. Flow-aided path following of an underwater robot. In *Proceedings of IEEE International Conference on Robotics and Automation (ICRA)*, pages 4602–4607, 2013.
- [19] J. A. Kleppe, J. G. Olin, and R. K. Menon. *Mechanical Variables Measurement – Solid, Fluid, and Thermal*, chapter Point velocity measurement. CRC Press, 2000.
- [20] A. G. P. Kottapalli, M. Asadnia, J. M. Miao, G. Barbastathis, and M. S. Triantafyllou. A flexible liquid crystal polymer mems pressure sensor array for fish-like underwater sensing. *Smart Materials and Structures*, 21(11), 2012.
- [21] F. D. Lagor, L. D. DeVries, K. M. Waycho, and D. A. Paley. Bio-inspired flow sensing and control: Autonomous underwater navigation using distributed pressure measurements. In *The 18th International Symposium on Unmanned Untethered Submersible Technology*, 2013.
- [22] J. C. Liao, D. N. Beal, G. V. Lauder, and M. S. Triantafyllou. Fish exploiting vortices decrease muscle activity. *Science*, 302:1566–1569, 2003.
- [23] P. Ligeza. Use of natural fluctuations of flow parameters for measurement of velocity vector. *IEEE Transactions on Instrumentation and Measurement*, 63, March 2014.
- [24] A. Lohrmann, R. Cabrera, and N. Kraus. Acoustic-doppler velocimeter (adv) for laboratory use. *Fundamentals and Advancements in Hydraulic Measurements and Experimentation Proceedings*, 15, 1994.
- [25] L. Lourenco and A. Krothapalli. On the accuracy of velocity and vorticity measurements with piv. *Experiments in Fluids*, 18:421 – 428, 1995.
- [26] B. J. MacVicar, E. Beaulieu, V. Champagne, and A. G. Roy. Measuring water velocity in highly turbulent flows: field tests of an electromagnetic current meter (ecm) and an acoustic doppler velocimeter (adv). *Earth Surface Processes and Landforms*, 32:1412 – 1432, 2007.
- [27] J. Mogdans and H. Bleckmann. Coping with flow: behavior, neurophysiology and modeling of the fish lateral line system. *Biological Cybernetics*, 106:627–642, 2012.
- [28] N. Mori, T. Suzuki, and S. Kakuno. Noise of acoustic doppler velocimeter data in bubbly flows. *Journal of Engineering Mechanics*, 133:122 – 125, 2007.
- [29] T. Pitcher, B. Partridge, and C. Wardle. A blind fish can school. *Science*, 194:963–965, 1976.
- [30] M. Plutowski. Survey: Cross-validation in theory and in practice. Dept. of Computational Science Research Report, Princeton, 1996.
- [31] D. Poggi, A. Porporato, and L. Ridolfi. An experimental contribution to near-wall measurements by means of a special laser doppler anemometry technique. *Experiments in Fluids*, 32:366 – 375, 2002.
- [32] Sergio De Ponte, S. Malavasi, Gianluca Galzerano, and C. Svelto. Novel particle image velocimetry system based on three-color pulsed lamps and image processing. *IEEE Transactions on Instrumentation and Measurement*, 53:175–180, Feb 2004.
- [33] A. Quattieri, F. Rizzi, G. Epifani, A. Ernits, M. Kruusmaa, and M. De Vittorio. Parylene-coated bioinspired artificial hair cell for liquid flow sensing. *Microelectronic Engineering*, 98:516–519, 2012.
- [34] A. Quattieri, F. Rizzi, M. T. Todaro, A. Passaseo, R. Cingolani, and M. De Vittorio. Stress-driven AlN cantilever-based flow sensor for fish lateral line system. *Microelectronic Engineering*, 88:2376–2378, 2011.
- [35] L. Ristroph, J. C. Liao, and J. Zhang. Lateral line layout correlates with the differential hydrodynamic pressure on swimming fish. *Physical Review Letters*, 114, 2015.
- [36] T. Salumäe and M. Kruusmaa. Flow-relative control of an underwater robot. *Proceedings of the Royal Society A*, 469, 2013.
- [37] C. Saunders, A. Gammerman, and V. Vovk. Ridge regression learning algorithm in dual variables. In *15th International Conference on Machine Learning (ICML)*, pages 515–521, 1998.
- [38] T. Shizhe. Underwater artificial lateral line flow sensors. *Microsystem Technologies*, 20(12):2123–2136, 2014.
- [39] I. Silicon Microstructures. Ultra small pressure sensor: SM5420C. Technical report, Silicon Microstructures, Inc., California, USA, 2013.
- [40] L. Simon, O. Richoux, A. Degroot, and L. Lionet. Laser doppler velocimetry for joint measurements of acoustic and mean flow velocities: Lms-based algorithm and crb calculation. *IEEE Transactions on Instrumentation and Measurement*, 57:1455–1464, 2008.
- [41] V.L. Streeter, E.B. Wylie, and Bedford K.W. *Fluid Mechanics*. McGraw-Hill, 1998.
- [42] S. M. van Netten and M. J. McHenry. The biophysics of the fish lateral line. In *The Lateral Line System*, pages 99–119. Springer New York, 2014.
- [43] R. Venturelli, O. Akanyeti, F. Visentin, J. Jezov, L. Chambers, G. Toming, J. Brown, M. Kruusmaa, W. M Megill, and P. Fiorini. Hydrodynamic pressure sensing with an artificial lateral line in steady and unsteady flows. *Bioinspiration and Biomimetics*, 7, 2012.
- [44] X. Wenjun and B. Peng. A pressure sensor calibration model based on support vector machine. In *The 24th Chinese Control and Decision Conference (CCDC)*, pages 3239–3242, May 2012.
- [45] J. Westerweel. Fundamentals of digital particle image velocimetry. *Measurement Science and Technology*, 8(12), 1997.
- [46] D. Xu and Y. Liu. A temperature compensation algorithm of piezoresistive pressure sensor and software implementation. In *IEEE International Conference on Mechatronics and Automation (ICMA)*, pages 1738–1742, Aug 2013.
- [47] Y. Yang, J. Chen, J. Engel, S. Pandya, N. Chen, C. Tucker, S. Coombs, D. L. Jones, and C. Liu. Distant touch hydrodynamic imaging with an artificial lateral line. *Proceedings of National Academy of Sciences of the United States of America*, 103:18891–18895, 2006.
- [48] F. Zhifang, J. Chen, J. Zou, D. Bullen, C. Liu, and F. Delcomyn. Design and fabrication of artificial lateral line flow sensors. *Journal of Micromechanics and Microengineering*, 12, 2002.
- [49] G. Zhou, Y. Zhao, and F. Guo. A temperature compensation system for silicon pressure sensor based on neural networks. In *The 9th IEEE International Conference on Nano/Micro Engineered and Molecular Systems (NEMS)*, pages 467–470, April 2014.

ACKNOWLEDGMENT

The research leading to these results has received funding from BONUS, the joint Baltic research and development programme, cofinanced by the European Union’s Seventh Framework Programme (20072013) under the BONUS Implementation Agreement. National funding for this work has been provided by the Academy of Finland (under the grant 280715), the German Federal Ministry for Education and Research (BMBF FKZ:03F0687A), and the Estonian Environmental Investment Centre (KIK P.7254 C.3255).